scientific reports

OPEN

2D layered SiP as anisotropic nonlinear optical material

Huseyin Sar, Jie Gao✉ & Xiaodong Yang✉

Two-dimensional (2D) material of silicon phosphide (SiP) has recently been shown as a promising optical material with large band gap, fast photoresponse and strong anisotropy. However, the nonlinear optical properties of 2D SiP have not been investigated yet. Here, the thickness-dependent in-plane anisotropic third-harmonic generation (THG) from the mechanically exfoliated 2D layered SiP flakes is reported. The crystal orientation of the SiP flake is determined by the angle-resolved polarized Raman spectroscopy. The angular dependence of the THG emission with respect to the incident linear polarization is found to be strongly anisotropic with the two-fold polarization dependence pattern. Furthermore, the effect of the SiP flake thickness on the THG power is analyzed.

The era of 2D layered materials, also known as van der Waals materials, has begun by the exfoliation of bulk graphite into monolayer graphene with extraordinary properties[1]. Beyond graphene, 2D materials such as transition metal dichalcogenides (TMDs) like MoS_2 and WSe_2, halides (MX_2 with X being Cl, Br, I[2]) and carbides/nitrides (MXenes[3–5]) have gained more attraction due to their superior electrical, optical, mechanical, thermoelectric, energy storage and sensing properties. Owing strong light-material interaction with broad spectral coverage range and tunable band gap, 2D materials are endorsed as promising optical materials. Besides to the linear optical properties, 2D materials are becoming prominent as promising nonlinear optical materials because of the high power conversion efficiency and large nonlinear optical susceptibility. Therefore, 2D materials have been accounted on several nonlinear optical applications including third-harmonic generation[6,7], second-harmonic generation (SHG), self-phase modulation[8,9], nonlinear Kerr effect[10,11], and four-wave mixing (FWM)[12]. Furthermore, 2D materials with low crystal symmetry such as BP[13], GeSe[14], GeAs[15], ReS[2,16] and SnSe[2,17] provide the opportunities for controlling the anisotropic physical properties with respect to the in-plane crystal orientation, giving a new degree of freedom for the angle-dependent manipulation. The anisotropic optical response empowers many novel photonic devices such as polarization sensors[18], synaptic devices[19], polarization sensitive photodetectors[20,21], and directional memories[22]. The integration of these anisotropic 2D materials with strong nonlinear optical responses into the photonic devices is important in the development of future nanoscale on-chip optical circuits[23] and quantum photonics[24].

In this manner, SiAs, GeAs, $GeAs_2$, GeAs, GeP and SiP as the members of a novel group IV-V 2D semiconductor family have gained a growing attention[25–27] due to their promising linear optical properties and low crystal symmetries. Specifically, SiP has been shown as an excellent optical material with a large band gap of 1.71 eV, fast photoresponse and strong anisotropy[28,29]. However, the intrinsic nonlinear optical properties of 2D layered SiP have not been investigated yet. In this study, the strong in-plane anisotropic THG in the exfoliated SiP flakes with different thicknesses is investigated. The angle-resolved polarized Raman spectra and the anisotropic THG responses of SiP thin flakes are measured and analyzed systematically. The effect of the SiP flake thickness on the THG power is also investigated experimentally and the extinction coefficient of SiP at the THG wavelength of 520 nm is estimated by theoretical analysis.

Results

Determination of SiP crystal orientation with Raman spectroscopy.

The in-plane anisotropic optical properties of SiP are a result of its low lattice symmetry. As a member of the group IV-V 2D semiconductor family, SiP exhibits the orthorhombic lattice with $Cmc2_1$ space group. The individual monolayers of SiP are held together by weak van der Waals interactions along the c-axis with an AB stacked layers to form the multilayer structure[30]. The perspective view of SiP crystal lattice is depicted in Fig. 1a, while the side view and top view of a SiP monolayer are depicted in Fig. 1b. The armchair and zigzag edge terminations along b-axis and a-axis are also illustrated in Fig. 1b.

Figure 1c shows the optical reflection microscope image of a mechanically exfoliated SiP flake with the laboratory frame x- and y-axes. The angle-resolved polarized Raman spectroscopy measurements are used to

Department of Mechanical and Aerospace Engineering, Missouri University of Science and Technology, Rolla, MO 65409, USA. ✉email: gaojie@mst.edu; yangxia@mst.edu
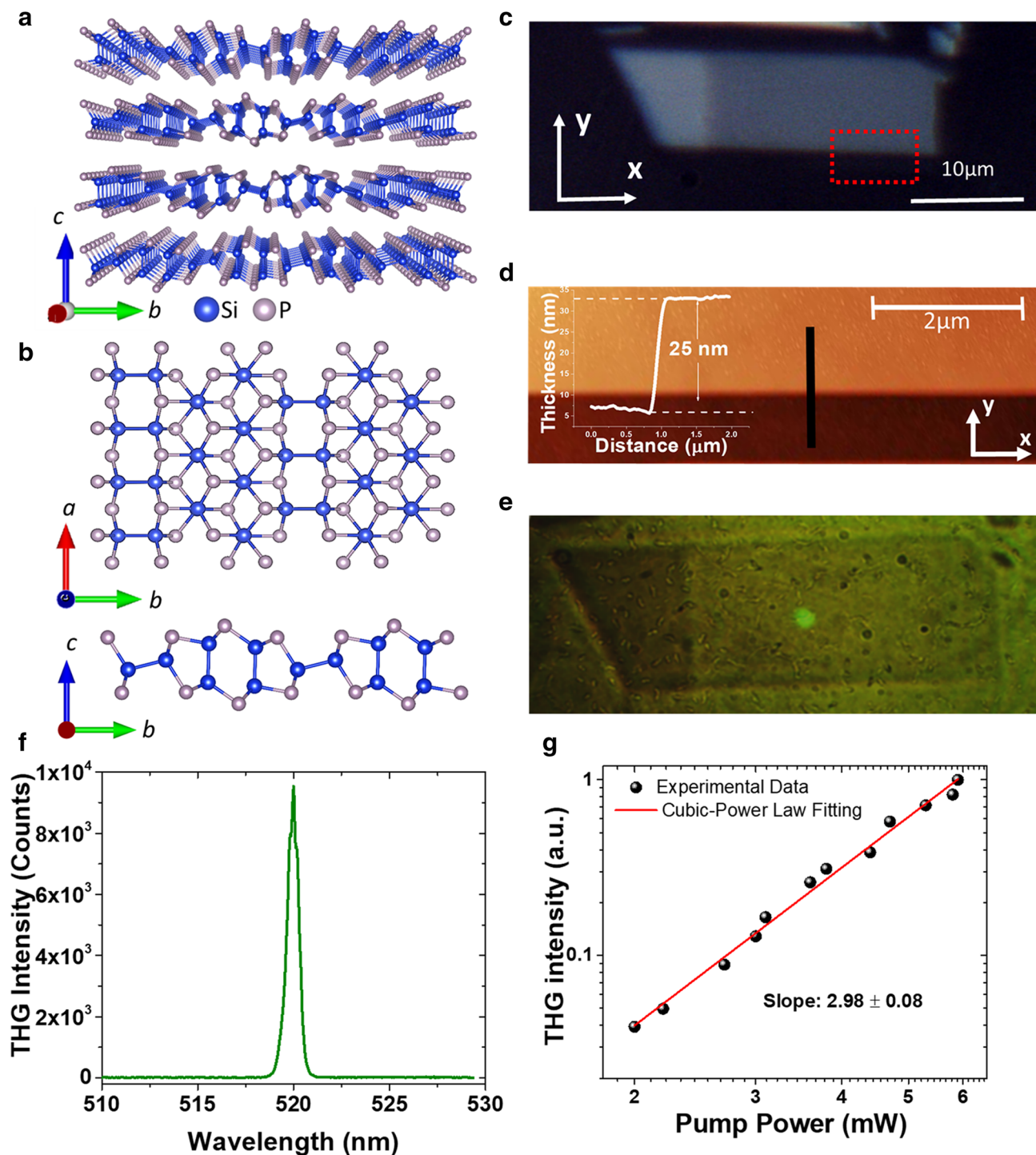
Figure 1. (**a**) The perspective view schematic of the crystal structure of 2D SiP. (**b**) The top view and side view schematics of a SiP monolayer. (**c**) The optical reflection microscope image of one exfoliated SiP flake with the laboratory axes *x* and *y*. Scale bar is 10 μm. The red dashed rectangle represents the region that the AFM is measured. (**d**) The AFM image of the SiP flake with the height profile through the black line as the inset figure. Scale bar is 2 μm. (**e**) The optical transmission microscope image of the flake with the green THG emission spot. (**f**) The spectrum of THG emission with the emission wavelength of 520 nm by using the 1560 nm pulsed laser excitation. (**g**) The measured THG emission intensity as a function of the incident pump power (black spheres) with the cubic-power law fitting curve (solid red line).
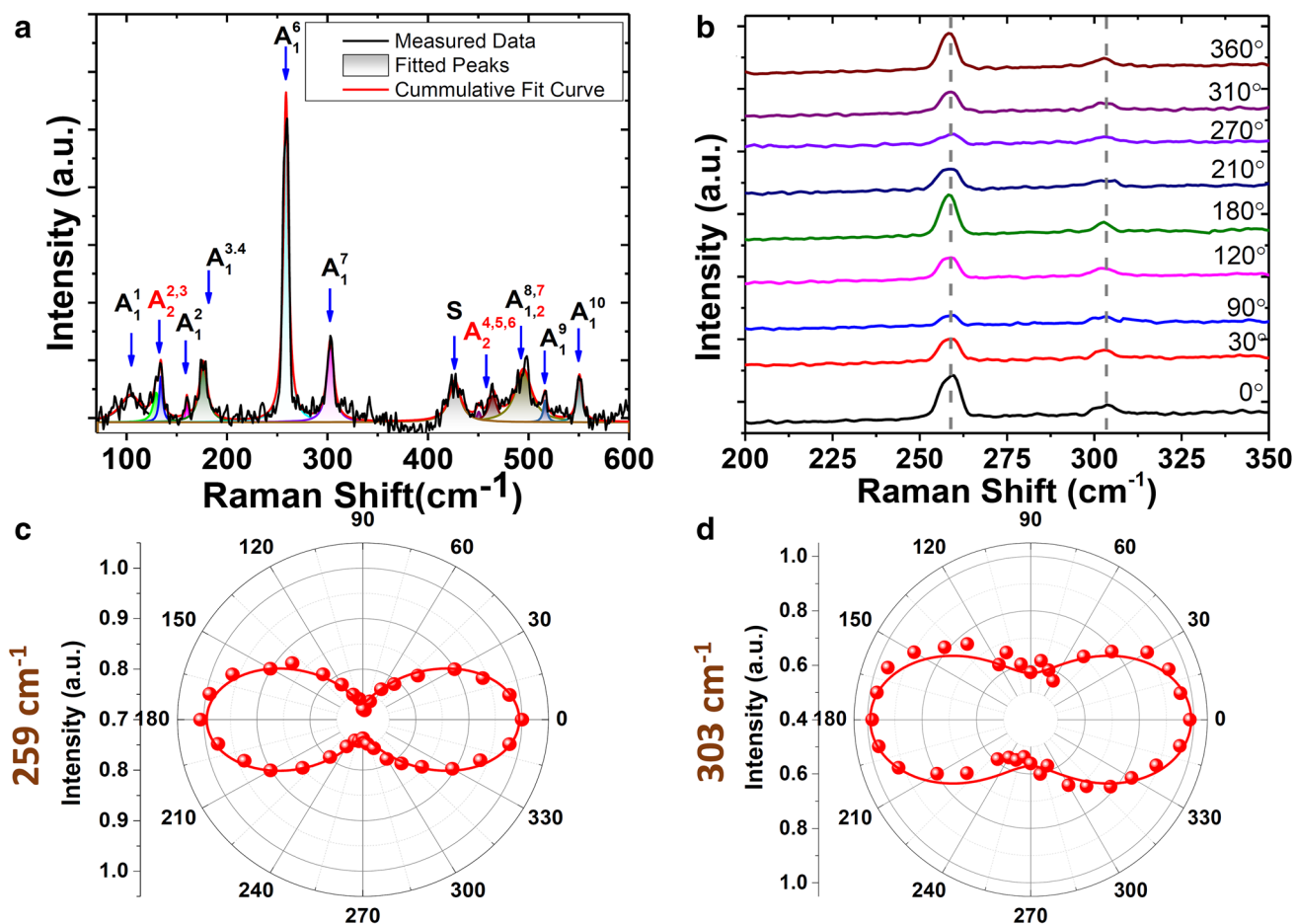
Figure 2. (**a**) The total Raman spectrum measured from the exfoliated 25 nm-thick SiP flake. (**b**) The angle-resolved polarized Raman spectra of the SiP flake acquired in the parallel configuration for different pump polarization angles. (**c**), (**d**) the polar plots of the Raman intensities of A_1^6 ($259cm^{-1}$) and A_1^7 ($303cm^{-1}$). The red spheres are the experimental data and the solid curves correspond to the data fitting by Eq. (2).

determine the armchair direction (b-axis) and zigzag direction (a-axis), where x- and y-axes are assigned as the armchair and zigzag directions accordingly. The thickness and surface characterization of the exfoliated SiP flakes are evaluated by the atomic force microscopy (AFM) measurements, as shown in Fig. 1d. The height profile extracted from the black line on the AFM image is shown as the inset of Fig. 1d, and the flake thickness is 25 nm. Figure 1e is the optical transmission microscope image of the flake, with the green THG emission spot excited by a 1560 nm pulsed pump laser with the spot size of 2.5 μm. The typical THG emission spectrum is shown in Fig. 1f where the emission wavelength is 520 nm. The cubic power-law dependence of the THG emission as a function of the pump power plotted in Fig. 1g is another proof of the THG process. The fitting is well achieved with a slope of 2.98 ± 0.08, confirming the occurrence of THG emission.

In Fig. 2a, the measured total Raman spectrum from the 25 nm-thick SiP flake is plotted, where the analyzer after the sample is removed. Since the measurements are carried out on a thin flake with the thickness of 25 nm, the Raman intensities of some modes are weak. In order to extract the exact Raman mode shifts and intensity values, each Raman mode has been fitted by a Gaussian function as shown in Fig. 2a. The Raman active modes of 2D layered SiP are along different atomic displacement directions in the ab-plane. Here, the estimated peak centers of Raman modes belonging to the vibrational direction along b-axis are 104.3, 176.42, 258.72, 302.66, 494.41, 516.46, and $550.71cm^{-1}$ which are assigned as A_1^1 to A_1^{10} modes, while the estimated peak centers of Raman modes belonging to the atomic displacement direction along a-axis are 129.54, 134.22, 426.12, 450.32, and $464.43cm^{-1}$ which are assigned as A_2^1 to A_2^7 modes. At this point, $A_1^{3,4}$, $A_2^{2,3}$, $A_2^{4,5,6}$ and $A_1^{8,7}$ modes refer to the overlapped Raman modes due to the adjacent vibration frequencies and weak intensities. These observed Raman modes match well with the previously reported Raman spectrum of SiP[28,31]. The Raman spectrum is not just utilized as the material defining tool but also used to determine the crystal orientation by resolving the polarization dependence behavior of the Raman modes. In this manner, the angle-resolved polarized Raman spectroscopy is commonly used to determine the crystal orientation[15,32–35]. Here, the parallel configuration in the angle-resolved polarized Raman spectroscopy is utilized where the analyzer direction is set to be parallel with the excitation polarization direction. The SiP flake sample is fixed with the assigned x and y laboratory axes as depicted in Fig. 1c. The laser beam polarization is varied by rotating a half-wave plate to sweep the angle θ relative to x-axis from 0° to 360° with a step of 10°. In Fig. 2b, the Raman spectra of the 25 nm-thick SiP thin flake for different laser

beam polarizations under the parallel configuration are plotted. The intensity variations of the Raman modes at $A_1^6: 259cm^{-1}$ and $A_1^7: 303cm^{-1}$ are shown to have a period of $180°$ which is an indication of the crystalline orientation dependency. On the other hand, the Raman mode frequencies are almost unchanged with respect to the incident laser polarization.

To further quantitatively analyze the periodical intensity variation of the strongest two Raman modes and determine the crystal orientation, the Raman selection rule is used to derivate the mode intensity function in the parallel configuration. The generalized form of Raman intensity is stated as:

$$I(j) = \left| d_i \cdot \overline{\overline{R}}(j) \cdot d_s^T \right| \tag{1}$$

where d_i and d_s refer to the unit polarization vectors of the incident and scattered light, j refers to the mode number and $\overline{\overline{R}}$ is the Raman tensor[36]. The intensities of A_1 and A_2 modes in the parallel configuration are expressed as:

$$I^\parallel(A_1) \propto \left(cos^2(\theta) + \frac{c_1}{c_2} \cdot sin^2(\theta) \cdot cos(\phi_{c_1c_2}) \right)^2 + sin^4(\theta) \cdot cos^2(\phi_{c_1c_2}) \tag{2}$$

$$I^\parallel(A_2) \propto |c|^2 \cdot sin^2(\theta) \cdot cos^2(\theta) \tag{3}$$

where c_1, c_2, and c are the constants of the Raman tensor, θ the linear polarization angle with respect to the crystal axis, and $\phi_{c_1c_2}$ represents the phase difference between c_1 and c_2. The angle-resolved Raman intensity variations of the $259cm^{-1}$ and $303cm^{-1}$ modes are shown as the polar plots in Fig. 2c,d, respectively. The red dots represent the experimental data and the red solid lines refer to the calculated Raman intensities from Eq. (2). The anisotropic Raman intensity variation shows a two-lobe pattern aligned along the armchair direction. As a result of that, the armchair and zigzag directions are assigned as x- and y-axes, respectively.

Anisotropic THG in exfoliated SiP flakes with different thicknesses.

The previously studied anisotropic linear optical properties of SiP foreshadows strong anisotropic nonlinear optical responses, which can be revealed by employing the angle-resolved THG measurements for different flake thicknesses. The THG emission along the armchair direction ($E_x^{3\omega}$) and the zigzag direction ($E_y^{3\omega}$) are measured by fixing the analyzer at $0°$ and $90°$ degrees, respectively. To quantitively analyze the THG emission and estimate the components of the third-order nonlinear susceptibility tensor $\chi_{im}^{(3)}$, the analytic expression of the emitted THG signal is derived by using the input field expression ($\mathbf{E}_I$) and the third-order nonlinear susceptibility tensor of the orthorhombic SiP crystal. The electric field intensity of the linearly polarized input pump beam with the fundamental frequency (ω) can be defined as:

$$\mathbf{E}_I = |\mathbf{E}|\widehat{r} \tag{4}$$

$$\widehat{r} = \widehat{x}\cos\theta + \widehat{y}\sin\theta \tag{5}$$

where θ is the polarization angle. The third-order nonlinear susceptibility tensor of SiP is expressed with the known crystal structure (orthorhombic) and space group (Cmc2$_1$) as[37,38]:

$$\chi_{im}^{(3)} = \begin{bmatrix} \chi_{11} & 0 & 0 & 0 & 0 & \chi_{16} & 0 & \chi_{18} & 0 & 0 \\ 0 & \chi_{22} & 0 & \chi_{24} & 0 & 0 & 0 & 0 & \chi_{29} & 0 \\ 0 & 0 & \chi_{33} & 0 & \chi_{35} & 0 & \chi_{37} & 0 & 0 & 0 \end{bmatrix} \tag{6}$$

where i equals to 1, 2, and 3 refers to x, y, z respectively, and m shows the mutual relation of the three components as follows:

$$\begin{array}{ccccccccccc} jkl & xxx & yyy & zzz & yzz & yyz & xzz & xxz & xyy & xxy & xyz \\ m & 1 & 2 & 3 & 4 & 5 & 6 & 7 & 8 & 9 & 0 \end{array} \tag{7}$$

As a result of x–y plane excitation, the components of $\chi_{im}^{(3)}$ with z terms are set to be zero. The THG electric field components will have only four non-zero terms left which is the result of removing z-axis dependent components. The resultant THG electric field expression is:

$$E^{3\omega} = \begin{bmatrix} E_x^{3\omega} \\ E_y^{3\omega} \\ E_z^{3\omega} \end{bmatrix} \propto \varepsilon_0 E^3 \begin{bmatrix} (\chi_{11}\cos^3\theta + 3\chi_{18}\cos\theta\sin^2\theta) \\ (\chi_{22}\sin^3\theta + 3\chi_{29}\sin\theta\cos^2\theta) \\ 0 \end{bmatrix} \tag{8}$$

Then the intensity of the emitted THG signal is written as:

$$I_x^{3\omega} \propto (E_x^{3\omega})^2 \propto \left(\chi_{11}\cos^3\theta + 3\chi_{18}\cos\theta\sin^2\theta \right)^2 \tag{9}$$

$$I_y^{3\omega} \propto (E_y^{3\omega})^2 \propto \left(\chi_{22}\sin^3\theta + 3\chi_{29}\sin\theta\cos^2\theta \right)^2 \tag{10}$$

In Fig. 3, the incident polarization angle-resolved THG emission plots of 2D SiP flakes with varying thicknesses from 10 to 85nm are shown, in which the strong anisotropic nonlinear optical response of the 2D SiP is clearly observed. For all the polar plots, $0°$ refers to the armchair direction and $90°$ refers to the zigzag direction.
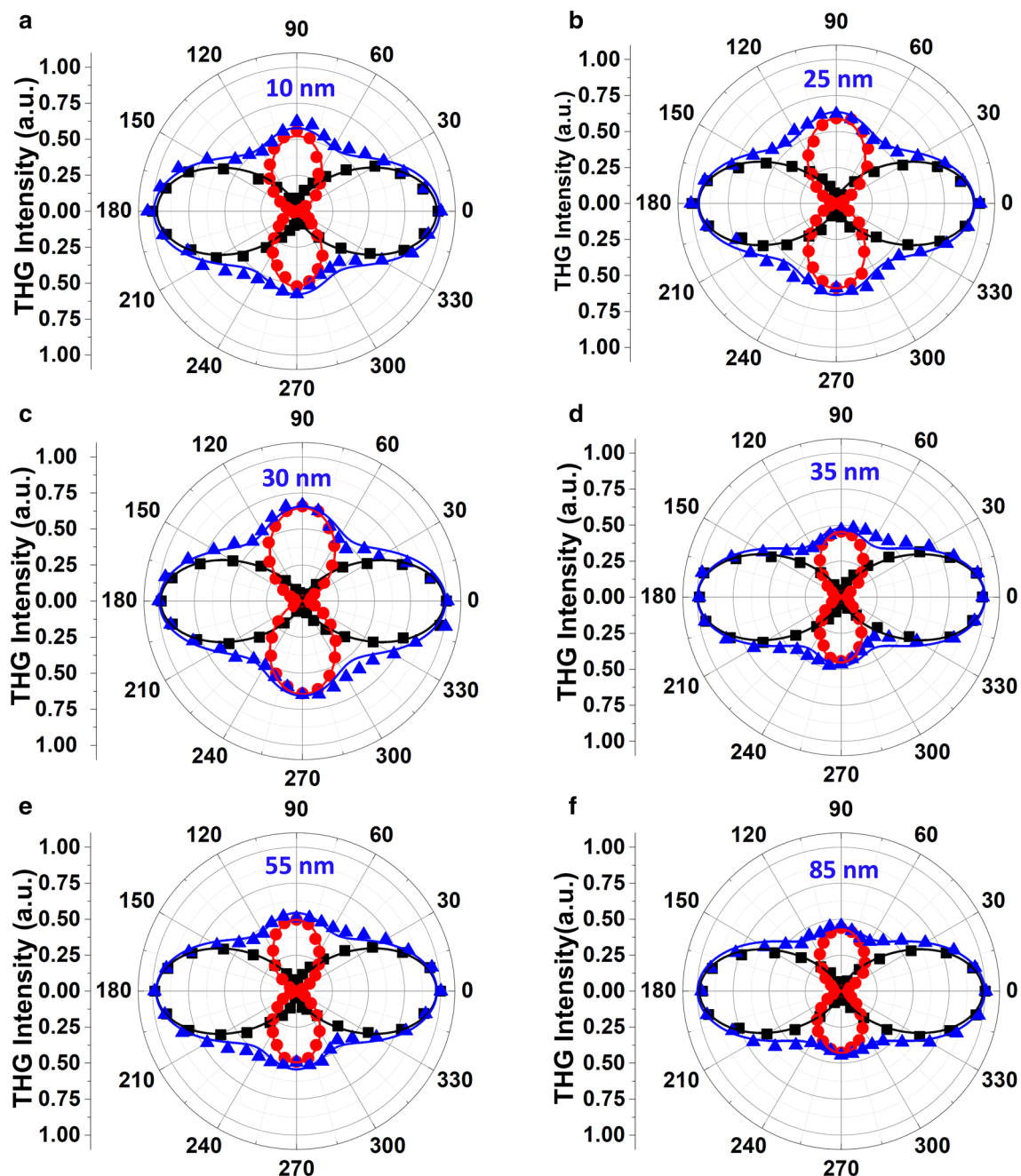
Figure 3. The angle-resolved THG intensity with respect to the incident linear polarization angle for the SiP flakes with thicknesses of **(a)** 10nm, **(b)** 25nm, **(c)** 30nm, **(d)** 35nm, **(e)** 55nm and **(f)** 85nm. The black squares, red circles and blue triangles represent the measured x-component, y-component and total THG intensity, respectively. Solid black, red and blue curves refer to the data fittings by Eqs. (9) and (10).

The black squares and red circles are the measured THG emission components along the armchair direction ($I_x^{3\omega}$) and the zigzag direction ($I_y^{3\omega}$) respectively, while the blue triangles represent the total THG emission ($I^{3\omega}$) with respect to the incident polarization angle. For all the flakes, the maximum THG signal is emitted as the input laser polarization is aligned along the armchair direction of the 2D SiP crystal, while the second maximum THG emission is occurred for the laser polarization along the zigzag direction of the crystal. The varying THG emission intensities for different incident polarization angles validate the strong anisotropic nonlinear optical response of 2D SiP. It is clearly shown that the input laser polarization angle where the maximum THG signal is obtained is in a perfect match with the angle of the armchair direction determined by the angle-resolved Raman measurements, manifesting that the nonlinear optical anisotropy of 2D SiP observed in THG measurements and the structural anisotropy determined by Raman measurements are in phase along the armchair and zigzag directions. Furthermore, the measured data is fitted by Eqs. (9) and (10) to estimate the components of the third-order nonlinear susceptibility tensor. The calculation results are depicted as the solid black, red and blue
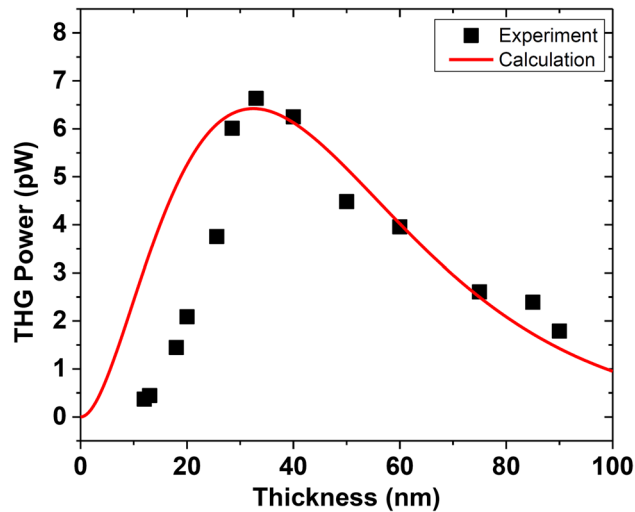
Figure 4. The dependence of THG emission power on the thickness of exfoliated SiP flake with the data fitting by Eq. (12). The black squares and solid red line refer to the experimental data and theoretical fitting, respectively.

lines which refer to the $I_x^{3\omega}$, $I_y^{3\omega}$ and $I^{3\omega}$ in Fig. 3. The calculated data matches well with the measured data. The exfoliated SiP flakes with thicknesses of 10, 25, 30, 35, 55 and 85nm exhibits very similar anisotropy patterns. All the flakes with different thicknesses show a two-fold polarization dependence pattern due to the unequal THG emission for the laser polarization along the armchair and zigzag directions. An average THG anisotropy ratio of 1.93 ± 0.44 is observed among the measurements for different thicknesses where the anisotropy ratio is quantized as the ratio of the maximum THG intensity to the second maximum one as $\left|I^{3\omega}\right|_{0°}/\left|I^{3\omega}\right|_{90°}$. The relatively high variation in THG anisotropic ratio can be addressed to the defects or strain which may be introduced during the mechanical exfoliation process. Such effects on the nonlinear optical properties has been previously observed for different nonlinear optical materials[13,16,39,40]. According to Eqs. (9) and (10), the third-order nonlinear susceptibility components also show anisotropy with the average χ_{11}/χ_{22} ratio of 1.38 ± 0.16. Furthermore, the THG conversion efficiency of SiP flakes with different thicknesses are measured for an average pump power of 3.6mW, corresponding to an excitation irradiance of 28.2GW/cm². The conversion efficiency for the SiP flake with 12 nm thickness is 1.02×10^{-10} which is the minimum conversion efficiency, while the conversion efficiency for the thickest flake with 90 nm thickness is measured as 6.56×10^{-10}. On the other hand, the maximum conversion efficiency is achieved for the 33 nm-thick SiP flake as 1.82×10^{-9} which is comparable to the reported THG conversion efficiencies for other kinds of anisotropic 2D materials including GeAs (1.1×10^{-9} for an irradiance of 8.4GW/cm²)[15], GeSe (2.7×10^{-9} for an irradiance of 5.6GW/cm²)[41], BP (2.8×10^{-9} for an irradiance of 440GW/cm²)[40] and ReS₂ (0.2×10^{-9} for a irradiance of 130GW/cm²)[16], as well as graphene (3×10^{-9} for an irradiance of 186GW/cm²)[6].

Figure 4 plots the THG emission power as a function of the thickness of exfoliated SiP flake. The thickness dependence trend can be explained by two mechanisms. The first mechanism is the rapid increase of THG power in the thickness range of 12 to 33nm which is a result of the cumulative contribution of the increased SiP layer number. However, the second mechanism is the exponential depletion of THG emission as the thickness increases from 33 to 90nm, which is related to the increased optical propagation length through the thick SiP flake that results in the domination of strong optical absorption. To further intuitively understand the effect of the flake thickness on the THG power and estimate the extinction coefficient, the THG power with respect to the flake thickness can be derived by solving the nonlinear Maxwell's equations as[13]:

$$P^{3\omega}(d) = \frac{9\omega^2 d^2}{16\sqrt{n_3^2 + k^2}\, n_1^3 \epsilon_0^2 c^4} \left|\chi^{(3)}\right|^2 \frac{(P^\omega)^3}{f^2 W^4 \tau^2 \left[\frac{\pi}{4\ln 2}\right]^3} \left(\frac{e^{-\frac{4\pi k d}{\lambda_3}} - 2\cos(\Delta k d)e^{-\frac{2\pi k d}{\lambda_3}} + 1}{d^2\left(\frac{4\pi^2 k^2}{\lambda_3^2} + \Delta k^2\right)}\right) e^{-\frac{4\pi k d}{\lambda_3}} \quad (11)$$

where d is the flake thickness, k is the extinction coefficient which is the imaginary part of refractive index at 3ω, n_1 and n_3 are the real parts of refractive indices at the fundamental and THG wavelengths, P^ω is the average pump power, $\Delta k = \frac{6\pi}{\lambda}(n_1 - n_3)$ is the phase mismatch between the forward propagating fundamental and the third-harmonic signal, and the pulsed pump laser parameters include beam width W, pulse width τ, and repetition rate f. With the constant average pump power P^ω, Eq. (11) can be further simplified as:

$$P^{3\omega}(d) \approx A d^2 \exp\left(-\frac{4\pi k d}{\lambda_3}\right) \quad (12)$$

where A is a constant. The measured THG power is fitted by Eq. (12) as the solid red line in Fig. 4, which gives the estimated extinction coefficient $k = 2.55$ at the THG wavelength of 520nm for the exfoliated SiP thin flakes. It is observed that for SiP flakes having small thicknesses less than 30 nm, the measured THG power shows the same trend as the fitted data, but the measured values are lower than the fitted ones. One potential explanation for this discrepancy is that the mechanical exfoliation and transfer process of SiP thin flakes from tape to glass substrate may affect several top surface layers negatively, which represents a large portion of the entire flake, so that the THG conversion efficiency is notably reduced for thin flakes less than 30 nm with weak THG responses. Another potential reason is the possible oxidation of the first few surface layers in SiP thin flakes exposed to ambient air, which also degrades the THG conversion efficiency. Future investigations using clean exfoliation in inert environment and surface passivation to effectively protect the SiP surface layers against the possible defects and ambient oxidation, and thus preserve their pristine structural and optical characteristics could potentially solve such discrepancy issue.

Discussion. In summary, the strong anisotropic nonlinear optical properties of the mechanically exfoliated 2D SiP flakes with different thicknesses are investigated in terms of the THG process. The angle-resolved polarized Raman spectroscopy is used to confirm the Raman signature of 2D SiP, determine the crystal orientation, and define the armchair and zigzag edge configurations of 2D SiP by using anisotropic Raman mode analysis. The angle-resolved THG emission with respect to the incident pump polarization angle is found to be strongly anisotropic with the two-fold polarization dependence pattern. The consistency of the anisotropic THG emission from SiP flakes with different thicknesses is revealed by the angle-resolved THG emission analysis. Furthermore, the THG conversion efficiency from the exfoliated SiP flakes with different thicknesses is also measured. The effect of the SiP flake thickness on the THG emission power is analyzed by the derived expression, where the extinction coefficient of SiP thin flakes at the THG wavelength is estimated and the optimal thickness for high conversion efficiency is revealed. The reported anisotropic nonlinear optical properties of 2D layered SiP shows its great potential as a nonlinear optical material used for future photonic integrated circuits and quantum chips.

Methods
Sample preparation.
The bulk SiP single crystal (2D Semiconductors) is mechanically exfoliated to isolate SiP thin flakes on the pre-cleaned glass cover slip substrate by the Nitto tape (SPV 224). The glass cover slip substrate is cleaned with the aid of sonication in acetone, isopropanol alcohol and deionized water.

Angle-resolved Raman spectroscopy measurements.
The total Raman spectrum and the angle-resolved polarized Raman spectra are measured by a home-built optical setup with a 632.8nm He–Ne laser. The laser beam passes through a linear polarizer and a half-wave plate to set the linear polarization before the sample. The laser beam is then focused on the sample by a 60×objective lens ($NA = 0.85$). A linear polarization analyzer is used after the sample to select the parallel polarization component of the Raman spectrum. The back-reflected signal is collected by the same objective lens and sent to the spectrometer. The excitation laser is blocked by a Rayleigh band rejection filter (Semrock, LP02-633RE-25) before the spectrometer.

Angle-resolved THG measurements.
The excitation source for THG measurements is chosen as a femtosecond pulsed laser at 1560nm with a spot size of 2.5μm (Calmer fiber laser, pulse width 90fs, repetition rate 80MHz). The input laser polarization is manipulated by a combination of a linear polarizer and a half-wave plate before the sample, while the output THG emission is passed through an analyzer after the sample. The pulsed laser beam is focused on the sample using a 40×objective lens ($NA = 0.65$) and the emitted THG signal is collected using a 100×objective ($NA = 0.70$). The excitation pulse transmitted through the sample is blocked by a low pass filter and the signal is collected into a spectrometer (Horiba, iHR 520) for the measurements.

References
1. Novoselov, K. S. *et al.* Electric field effect in atomically thin carbon film. *Science* **306**, 666–669 (2004).
2. Kulish, V. V. & Huang, W. Single-layer metal halides MX2 (x= cl, br, i): Stability and tunable magnetism from first principles and monte carlo simulations. *J. Mater. Chem.* **5**, 8734–8741 (2017).
3. Gao, G., O'Mullane, A. P. & Du, A. 2D mxenes: A new family of promising catalysts for the hydrogen evolution reaction. *ACS Catal.* **7**, 494–500 (2017).
4. Anasori, B., M. Lukatskaya, R., & Gogotsi, Y., 2D metal carbides and nitrides (Mxenes) for energy storage. *Nat. Rev. Mater.* **2**, 1–17 (2017).
5. Sar, H. *et al.* MoS2 phototransistor sensitized by colloidal semiconductor quantum wells. *Adv. Opt. Mater.* https://doi.org/10.1002/adom.202001198 (2020).
6. Saynatjoki, A. *et al.* Rapid large-area multiphoton microscopy for characterization of graphene. *ACS Nano* **7**, 8441–8446 (2013).
7. Nasari, H. & Abrishamian, M. S. Electrically tunable, plasmon resonance enhanced, terahertz third harmonic generation via graphene. *RSC Adv.* **6**, 50190–50200 (2016).
8. Wu, R. *et al.* Purely coherent nonlinear optical response in solution dispersions of graphene sheets. *Nano Lett.* **11**, 5159–5164 (2011).
9. Vermeulen, N. *et al.* Negative Kerr nonlinearity of graphene as seen via chirped-pulse-pumped self-phase modulation. *Phys. Rev. Appl.* **6**, 044006 (2016).
10. Yang, H. *et al.* Giant two-photon absorption in bilayer graphene. *Nano Lett.* **11**, 2622–2627 (2011).
11. Yu, S. *et al.* All-optical graphene modulator based on optical Kerr phase shift. *Optica* **3**, 541–544 (2016).
12. Wu, Y. *et al.* Generation of cascaded four-wave-mixing with graphene-coated microfiber. *Photonics Res.* **3**, A64–A68 (2015).

13. Youngblood, N., Peng, R., Nemilentsau, A., Low, T. & Li, M. Layer-tunable third-harmonic generation in multilayer black phosphorus. *ACS Photonics* **4**, 8–11 (2017).
14. Zhou, X. *et al.* Highly anisotropic GeSe nanosheets for phototransistors with ultrahigh photoresponsivity. *Adv. Sci.* **5**, 1800478 (2018).
15. Sar, H., Gao, J. & Yang, X. In-plane anisotropic third-harmonic generation from germanium arsenide thin flakes. *Sci. Rep.* **10**, 1–10 (2020).
16. Cui, Q., Muniz, R. A., Sipe, J. E. & Zhao, H. Strong and anisotropic third-harmonic generation in monolayer and multilayer ReS2. *Phys. Rev. B* **95**, 165406 (2017).
17. Biswas, R. *et al.* Third-harmonic generation in multilayer Tin Diselenide under the influence of Fabry-Perot interference effects. *Opt. Express* **27**, 28855–28865 (2019).
18. Tan, C. *et al.* High-yield exfoliation of ultrathin two-dimensional ternary chalcogenide nanosheets for highly sensitive and selective fluorescence DNA sensors. *J. Am. Chem. Soc.* **137**, 10430–10436 (2015).
19. Tian, H. *et al.* Anisotropic black phosphorus synaptic device for neuromorphic applications. *Adv. Mater.* **28**, 4991–4997 (2016).
20. Yuan, H. *et al.* Polarization-sensitive broadband photodetector using a black phosphorus vertical p–n junction. *Nat. Nanotechnol.* **10**, 707–713 (2015).
21. Liu, F. *et al.* Highly sensitive detection of polarized light using anisotropic 2D ReS2. *Adv. Funct. Mater.* **26**, 1169–1177 (2016).
22. Wang, H. *et al.* Gate tunable giant anisotropic resistance in ultra-thin GaTe. *Nat. Commun.* **10**, 1–8 (2019).
23. Witzens, J., Baehr-Jones, T. & Hochberg, M. On-chip OPOs. *Nat. Photonics* **4**, 10–12 (2010).
24. Obrien, J. L., Furusawa, A. & Vučković, J. Photonic quantum technologies. *Nat. Photonics* **3**, 687–695 (2009).
25. Mortazavi, B., Shahrokhi, M., Cuniberti, G. & Zhuang, X. Two-dimensional SiP, SiAs, GeP and GeAs as promising candidates for photocatalytic applications. *Coatings* **9**, 522 (2019).
26. Zhou, L., Guo, Y. & Zhao, J. GeAs and SiAs monolayers: Novel 2D semiconductors with suitable band structures. *Physica E Low Dimens. Syst. Nanostruct.* **95**, 149–153 (2018).
27. Li, L. *et al.* 2D GeP: An unexploited low-symmetry semiconductor with strong in-plane anisotropy. *Adv. Mater.* **30**, 1706771 (2018).
28. Li, C. *et al.* Highly sensitive detection of polarized light using a new group IV–V 2D orthorhombic SiP. *J. Mater. Chem. C* **6**, 7219–7225 (2018).
29. Xu, Y., Shi, Z., Shi, X., Zhang, K. & Zhang, H. Recent progress in black phosphorus and black-phosphorus-analogue materials: Properties, synthesis and applications. *Nanoscale* **11**, 14491–14527 (2019).
30. Cheng, A.-Q., He, Z., Zhao, J., Zeng, H. & Chen, R.-S. Monolayered silicon and germanium monopnictide semiconductors: excellent stability, high absorbance, and strain engineering of electronic properties. *ACS Appl. Mater. Interfaces* **10**, 5133–5139 (2018).
31. Huang, S. *et al.* In-plane optical anisotropy of layered gallium telluride. *ACS Nano* **10**, 8964–8972 (2016).
32. Feng, Y. *et al.* Raman vibrational spectra of bulk to monolayer ReS2 with lower symmetry. *Phys. Rev. B* **92**, 054110 (2015).
33. Nagler, P., Plechinger, G., Schüller, C. & Korn, T. Observation of anisotropic interlayer Raman modes in few-layer ReS2. *Phys. Status Solidi R* **10**, 185 (2016).
34. Wang, X. *et al.* Short-wave near-infrared linear dichroism of two-dimensional germanium selenide. *J. Am. Chem. Soc.* **139**, 14976–14982 (2017).
35. Yang, S. *et al.* Highly in-plane optical and electrical anisotropy of 2D germanium arsenide. *Adv. Funct. Mater.* **28**, 1707379 (2018).
36. Loudon, R. The raman effect in crystals. *Adv. Phys.* **13**, 423–482 (1964).
37. Boyd, R. W. *Nonlinear optics* (Academic Press, 2019).
38. Yang, X. L. & Xie, S. W. Expression of third-order effective nonlinear susceptibility for third-harmonic generation in crystals. *Appl. Opt.* **34**, 6130–6135 (1995).
39. Rodrigues, M. J. L. F. *et al.* Resonantly increased optical frequency conversion in atomically thin black phosphorus. *Adv. Mater.* **28**, 10693–10700 (2016).
40. Autere, A. *et al.* Rapid and large-area characterization of exfoliated black phosphorus using third-harmonic generation microscopy. *J. Phys. Chem. Lett.* **8**, 1343–1350 (2017).
41. Dasgupta, A., Gao, J. & Yang, X. Anisotropic third-harmonic generation in layered germanium selenide. *Laser Photonics Rev.* **14**, 1900416 (2020).

Acknowledgements

Author contributions

X. Y., J. G. and H. S. conceived the idea of the research. H. S. performed the experiments. X. Y. and J. G. directed the research. All authors discussed the results and contributed to the manuscript.

Competing interests

The authors declare no competing interests.

Additional information

Correspondence and requests for materials should be addressed to J.G. or X.Y.

Reprints and permissions information is available at www.nature.com/reprints.

Publisher's note Springer Nature remains neutral with regard to jurisdictional claims in published maps and institutional affiliations.